Lithium Niobate Photonic Crystal Nanocavities

CNF Project Number: 1997-11
Principal Investigator: Qiang Lin
Users: Hanxiao Liang, Mingxiao Li

Affiliation: Department of Electrical and Computer Engineering, University of Rochester
Primary Source of Research Funding: National Science Foundation (ECCS-1509749, ECCS-1610674)
Contact: qiang.lin@rochester.edu, hanxiao.liang@rochester.edu, mli53@ur.rochester.edu
Website: http://photonlab.hajim.rochester.edu/
Primary CNF Tools Used: JEOL 9500 electron-beam lithography, AJA ion mill

Abstract:

Lithium niobate, with its wide applications in optics and mechanics, is a chemically inert material, and fabrication techniques for microscale and nanoscale structures of lithium niobate are to be developed. In this report, we demonstrate fabricating high-quality lithium niobate 1D and 2D photonic crystal cavities, using electron beam lithography and ion milling. Our devices exhibit high optical *Q* factors, paving the way for cavity nonlinear optics and cavity opto-mechanics of lithium niobate.

Summary of Research:

Lithium niobate (LN) exhibits outstanding electro-optic, nonlinear optical, acousto-optic, piezoelectric, photorefractive, pyroelectric, and photoconductive properties, that have found very broad applications in telecommunication, nonlinear/quantum photonics, microelectromechanics, information storage and sensing, among many others. Recently, significant interest has been attracted to develop LN photonic devices on chip-scale platforms, which have shown significant advantage in device engineering compared with conventional approaches [1-4]. Miniaturization of device dimensions dramatically enhances optical field in the devices which enables a variety of nonlinear optical, quantum optical, and optomechanical functionalities. In our work, we demonstrate LN 1D and 2D photonic crystal with more than optical *Q* around 10^5, more than two orders of magnitude higher than other LN nanocavities reported to date. In our 1D LN photonic crystal, the high optical quality together with tight mode confinement leads to extremely strong nonlinear photorefractive effect, with a resonance tuning rate of ~ 0.64 GHz/aJ, or equivalently ~ 84 MHz/photon, three orders of magnitude greater than other LN resonators. In particular, we observed intriguing quenching of photorefraction that has never been reported before. The devices also exhibit strong optomechanical coupling with gigahertz nanomechanical mode with a significant $f \cdot Q$ product of 1.47×10^{12} Hz.

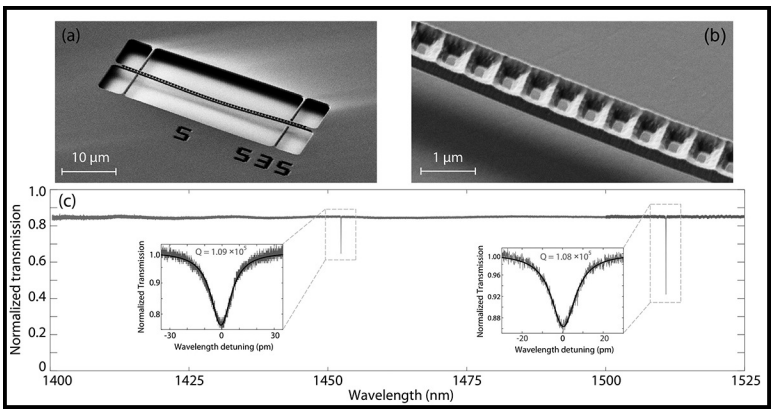

Figure 1: (a) (b) SEM images of a $LiNbO_3$ photonic crystal nanobeam. (c) Normalized transmission spectrum of the photonic crystal cavity, measured by two tunable lasers operating at different wavelength ranges (indicated as black and grey curves). Insets show detailed transmission spectra of the fundamental TE (TE0) mode and second-order TE (TE1) mode, respectively.

The fabrication process of our devices is pretty standard. First, we start with an X-cut lithium niobate-on-insulator wafer, which has a device layer of 300 nm sitting on a buried silicon oxide layer of 2 μm; then we spin ZEP-520A on the top of the wafer, and do patterning with JEOL 9500 electron beam lithography. Second, lithium niobate is etched with AJA ion milling, with ZEP-520A as the mask. Next, the remaining resist is removed by YES Asher oxygen plasma etcher. Finally, diluted hydrofluoric acid is utilized to remove buried silicon oxide and release our suspended structures.

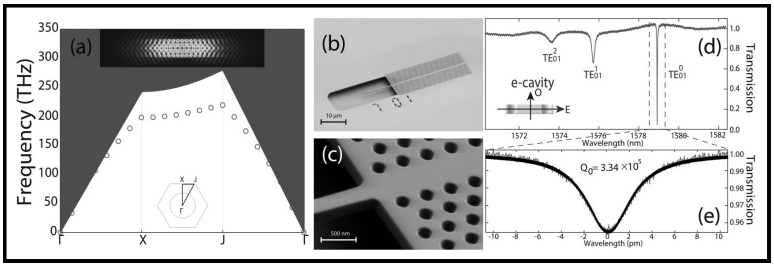

Figure 2: (a) Dispersion property of the fundamental transverse-electric-like (TE-like) guided mode inside the designed 2D photonic crystal slab. Optical mode field profiles of the fundamental mode are shown on the top. (b) Scanning electron microscopic image of a fabricated 2D LN PhC slab. (c) Zoom-in image of a section of the photonic crystal slab. (d) Laser-scanned transmission spectrum of an e-cavity. (e) Detailed transmission spectra of the fundamental cavity modes, with the experimental data shown in grey and the theoretical fitting shown in black.

Figure 1 (a)(b) shows the SEM images of a $LiNbO_3$ photonic crystal nanobeam, which show clearly the quality of device etching and dimension control. By launching a continuous-wave tunable laser into the cavity with a tapered optical fiber and monitoring the cavity transmission, we obtained the cavity transmission spectrum shown in Figure 1(c) for the transverse electric (TE) optical field with polarization lying in the device plane. Figure 1(c) shows two distinct cavity modes located at 1452 and 1511 nm, which correspond to the fundamental (TE0) and second-order (TE1) TE modes of the device, respectively. In particular, the two cavity modes exhibit optical Q as high as 1.09×10^5 and 1.08×10^5, respectively, which are more than two orders of magnitude higher than current state-of-the-art LN photonic crystal devices.

Figure 2 shows our design and fabrication result for our 2D LN photonic crystal. The dispersion property of the fundamental transverse-electric-like (TE-like) guided mode inside the designed 2D photonic crystal slab is shown in Figure 2 (a). Optical mode field profiles of the fundamental mode are shown on the top. The scanning electron microscopic image of a fabricated 2D LN PhC slab, shown in Figure 2 (b) and Figure 2 (c), indicates our high etching quality. For convenience, we denote the one perpendicular to the optical axis as an e-cavity since the dominant electric field polarizes along the optical axis, corresponding to the extraordinary polarization (Figure 2 (d)). Accordingly, we denote the one in parallel with the optical axis as an o-cavity as the dominant cavity field polarizes along the ordinary polarization. The highest Q we achieved in our O-cavity is 3.34×10^5. In particular, the peculiar anisotropy of photorefraction quenching and unique anisotropic thermo-optic nonlinear response have never been reported before.

In conclusion, we have developed the fabrication of high quality photonic crystal on lithium niobate-on-insulator platform using electron beam lithography and ion milling. High-quality etching of lithium niobate is verified by 1D photonic crystal nanocavities with Q of 10^5 and 2D photonic crystal nanocavities with Q of 3.34×10^5. Our work is of great potential for nonlinear optics, quantum photonics of lithium niobate on chip.

References:

[1] M. Roussey, et al., Appl. Phys. Lett. 89, 241110 (2006).

[2] G. Zhou and M. Gu, Opt. Lett. 31, 2783 (2006).

[3] N. Courjal, et al., Appl. Phys. Lett. 96, 131103 (2010).

[4] R. Geiss, et al., Appl. Phys. Lett. 97, 131109 (2010).

Lithium Niobate Nanophotonic Waveguides for Tunable Second-Harmonic Generation

CNF Project Number: 1997-11

Principal Investigator: Qiang Lin

Users: Rui Luo, Yang He

Affiliation: Department of Electrical and Computer Engineering, University of Rochester

Primary Sources of Research Funding: National Science Foundation (ECCS-1641099, ECCS-1509749), DARPA (W31P4Q-15-1-0007)

Contact: qiang.lin@rochester.edu, ruiluo@rochester.edu, yhe26@ur.rochester.edu

Website: http://photonlab.hajim.rochester.edu/

Primary CNF Tools Used: JEOL 9500 electron beam lithography, AJA ion mill

Abstract:

We report on-chip second-harmonic generation (SHG) that simultaneously achieves a large tunability and a high conversion efficiency inside a single device. We utilize the unique strong thermo-optic birefringence of LN to achieve flexible temperature tuning of type-I inter-modal phase matching. We experimentally demonstrate spectral tuning with a tuning slope of 0.84 nm/K for a telecom-band pump, and a nonlinear conversion efficiency of 4.7% W^{-1}, in a LN nanophotonic waveguide only 8 mm long.

Summary of Research:

Lithium niobate (LN) has attracted considerable attention in nonlinear optics for decades, due to its wide bandgap and large $\chi^{(2)}$ nonlinearity that support efficient second-harmonic generation (SHG), sum-/difference-frequency generation, and parametric down-conversion, which are conventionally enabled by quasi-phase matching in periodically-poled LN waveguides made from reverse proton exchange [1-3]. Recent advance in LN nonlinear photonics has shown the great advantages of the LN-on-insulator platform, which exhibits not only sub-micron mode confinement that enhances nonlinear conversion efficiencies, but also more degrees of freedom in waveguide geometry for dispersion engineering [4-8], which offer potentials for novel functionalities. Here, we demonstrate highly-efficient thermal control of phase-matched wavelengths for SHG in a LN nanophotonic waveguide, with a measured tuning slope of 0.84 nm/K for a telecom pump [9]. Our device is of great potential for on-chip wavelength conversion that produces highly-tunable coherent visible light, essential for various integrated photonic applications such as particle and chemical sensing in aqueous environments, while taking advantage of the mature telecom laser technology.

In order to effectively tune the phase-matching window of SHG, we need a controlling mechanism that is able to induce a significant relative change in effective indices at the two involved wavelengths. We take advantage of the large thermo-optic birefringence of LN, i.e.

$$\left|\frac{dn_e}{dT}\right| \gg \left|\frac{dn_o}{dT}\right|,$$

which allows us to introduce disparate index changes between two interband modes with orthogonal polarizations, by simply varying the temperature [10,11]. This effect is maximized on a Z-cut wafer, which supports high-purity polarization modes. Thus, in a Z-cut LN waveguide [see Figure 1(a)], we designed the geometry for phase matching between $TE_{0,\text{tele}}$ in the telecom and $TM_{2,\text{vis}}$ in the visible [see Figure 1(b)(c)]. As presented in Figure 1(d)(e), by simulation with the finite-element method (FEM) that takes temperature- and wavelength-dependent thermo-optic effects into account [10], we get a phase-matched pump wavelength λ_{PM} of around 1540 nm at T = 20°C, and it is shifted to 1574 nm at T = 70°C, with a fitted tuning slope of 0.69 nm/K [see Figure 1(f)].

To confirm our simulation results, we fabricated waveguides on a Z-cut LN-on-insulator wafer with electron-beam lithography and ion milling [6,9,11]. Scanning electron microscope (SEM) pictures [see Figure 2(a), insets] show very smooth sidewalls, indicating a low propagation loss. Then we conducted experiments for SHG, with the setup shown in Figure 2(a), where pump light from a continuous-wave tunable telecom laser is coupled into a LN waveguide via a lensed fiber, and collected together with the frequency-doubled

light by a second lensed fiber; after being separated from its second-harmonic by a 780/1550 WDM, the telecom pump light is directed to an InGaAs detector for monitoring, while the generated visible light is sent to a spectrometer for detection. We employed a waveguide with a length of about 8 mm. The fiber-to-chip coupling loss is about 5 dB/facet, and the waveguide propagation loss is estimated to be 0.54 dB/cm. By scanning the laser wavelength, we could find pump wavelengths that generate second-harmonic light.

As shown in Figure 2(b), at T = 18.7°C, significant SHG is achieved by pump light around 1559 nm, with a sinc^2-like spectrum, from which we extract a peak conversion efficiency of $4.7\%\text{W}^{-1}$. As we increase the device temperature, λ_{PM}, the phase-matched pump wavelength that exhibits the peak conversion efficiency, is gradually shifted to longer wavelengths.

As shown in Figure 2(c), the experimentally measured $d\lambda_{PM}/dT$ is 0.84 nm/K, which agrees very well with our simulation [see Figure 1(f)]. The larger experimental value potentially results from a positive contribution by pyroelectric and thermo-expansion effects that were not considered in the simulation.

References:

[1] M. M. Fejer, et al., IEEE J. Quantum Electron. 28, 2631 (1992).

[2] N. I. Yu, et al., Opt. Lett. 27, 1046 (2002).

[3] H. Jin, et al., Phys. Rev. Lett. 113, 103601 (2014).

[4] L. Chang, et al., Optica 3, 531 (2016).

[5] J. Lin, et al., Phys. Rev. Appl. 6, 014002 (2016).

[6] C. Wang, et al., Opt. Express 25, 6963 (2017).

[7] A. Rao, et al., Appl. Phys. Lett. 110, 111109 (2017).

[8] R. Luo, et al., Opt. Express 25, 24531 (2017).

[9] R. Luo, et al, arXiv:1804.03621 (2018).

[10] L. Morettia, et al., J. Appl. Phys. 98, 036101 (2005).

[11] R. Luo, et al., Opt. Lett. 42, 1281 (2017).

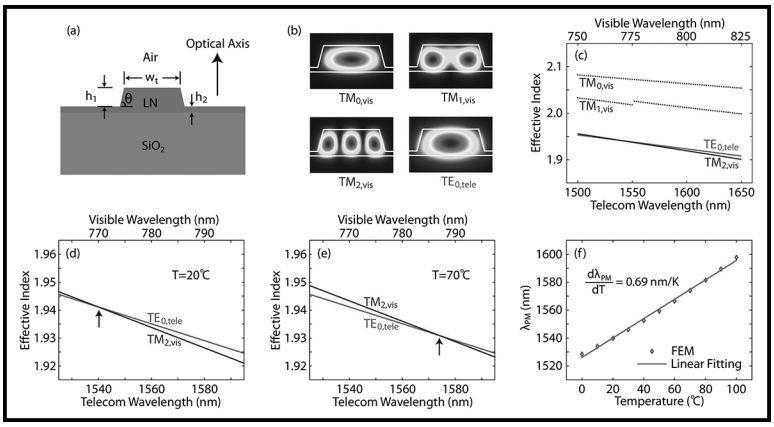

Figure 1: (a) Schematic of our Z-cut LN waveguide. FEM simulation of (b) mode profiles, and (c) effective indices as functions of wavelength, of $\text{TE}_{0,\text{tele}}$ in the telecom band and $\text{TM}_{j,\text{vis}}$ (j = 0, 1, 2) in the visible, where w_t = 1200 nm, h_1 = 460 nm, h_2 = 100 nm, and θ = 75°, at 20°C. The discontinuity in the effective index of $\text{TM}_{1,\text{vis}}$ is due to its coupling with $\text{TE}_{2,\text{tele}}$ (not shown). Zoom-in of the wavelength-dependent effective indices of $\text{TE}_{0,\text{tele}}$ and $\text{TM}_{2,\text{vis}}$ at (d) 20°C, and (d) 70°C, with black arrows indicating phase matching. (f) Simulated λ_{PM} as a function of temperature.

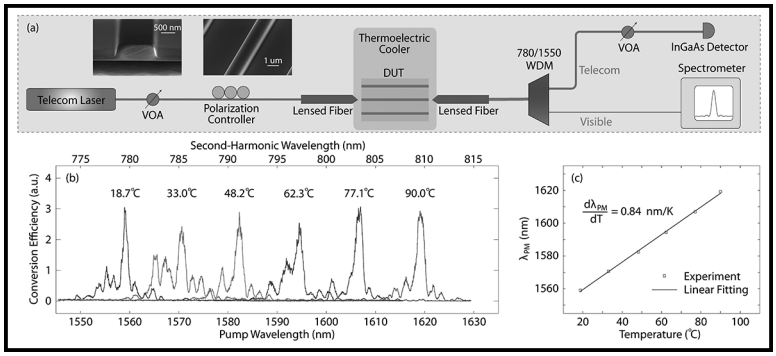

Figure 2: (a) Experimental setup. Insets are SEM pictures showing the waveguide facet and sidewall. (b) SHG spectrum at different temperature. (c) Measured λ_{PM} as a function of temperature.

Rabi-Like Oscillations in Photon Pair Correlations

CNF Project Number: 1997-11
Principal Investigator: Qiang Lin
User: Steven Rogers

Affiliation: Department of Physics and Astronomy, University of Rochester
Primary Source of Research Funding: National Science Foundation (Grant Number: ECCS-1351697)
Contact: qiang.lin@rochester.edu, steven.rogers@rochester.edu
Primary CNF Tools Used: JEOL 9500, UNAXIS 770, YES Asher

Abstract:

We have produced a new quantum coherence phenomenon via photon generation within ultra-high-*Q* silicon microdisks. The Rayleigh-scattering-induced strong coupling of counterpropagating modes opens up discrete energy pathways for pair creation, leading to Rabi-like oscillations in the biphoton second-order coherence. Additionally, the pump resonance splitting may be used to coherently control the internal structure of the oscillations by enabling the quantum interference between multiple creation pathways.

Summary of Research:

Optical microresonators have proven to be excellent chip-scale sources of heralded single photons and entangled photon pairs [1-3]. In this report, we will show that they possess a new and fascinating functionality not seen in any other system to date. We propose and demonstrate that the Rayleigh-scattering-induced strong coupling between counterpropagating cavity modes within microresonators can be used to achieve Rabi-like oscillations in the biphoton second-order coherence.

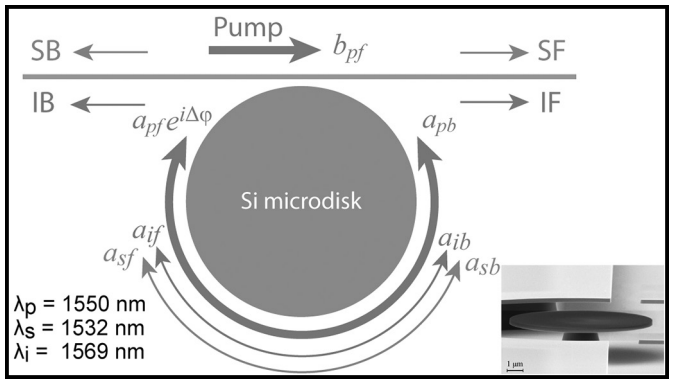

Figure 1: Illustration of the intracavity physics leading to oscillations in the biphoton correlations. The input pump field is evanescently coupled into intracavity pump mode, leading to spontaneous four-wave mixing. The intracavity fields are labeled as, a_{jk}, where j = p, s, i for pump, signal and idler, respectively, and k = f, b denotes forward and backward. Signal (S) and idler (I) photons are coupled from the optical cavity into the waveguide in the forward (F) and backward (B) directions, resulting in four path configurations for cross-correlations. The inset depicts a scanning electron microscope image of the suspended silicon microdisk.

Figure 1 illustrates the system and the intracavity processes that lead to this phenomenon. A scanning electron microscope image of the actual silicon microdisk is shown in the inset, with a radius of 4.5 μm, thickness of 260 nm and average intrinsic optical *Q*s above one million. The device pattern was defined using the JEOL 9500 electron beam lithography system and transferred to the silicon layer using the UNAXIS 770 etcher. A pump laser is evanescently coupled into the microdisk, wherein cavity-enhanced spontaneous four-wave mixing (SFWM) occurs between the pump (p), signal (s) and idler (i) modes. In the absence of a coupling mechanism, each cavity mode admits two degenerate eigenmodes, forward and backward traveling. However, the extreme enhancement of the light-matter interaction strength in our system enables the small Rayleigh scattering at the boundary of the cavity to induce a strong coupling between the forward and backward modes, which manifests as the well-known resonance splitting [4]. Thus, the single photons may coherently cycle between forward and backward modes, as depicted by the use of bidirectional arrows in Figure 1. The photons are coupled out of the cavity and detected by superconducting nanowire single-photon detectors. A coincidence counter histograms the detection of photon pairs as a function of their arrival time differences, which yields the biphoton coherence waveforms, $g^{(2)}(\tau)$, seen in Figures 2-4.

In analogy to the formation of dressed states in an atom-cavity system [5], the strong coupling between counterpropagating modes implies that it is no longer possible to describe forward or backward independently. And given that the biphoton coherence properties are

established by the cavity [6], we expect that the strong coupling must be imprinted on the biphoton correlations. This is precisely what we observe in Figures 2-4.

The measured biphoton correlations display a stunning difference compared with other chip-scale sources, which exhibit monotonically decaying profiles. In Figure 2, we see that at certain delay times the photon pairs in the signal forward-idler forward (SF-IF) channels are highly correlated, then diminish to nearly zero, before being revived in an oscillatory manner.

Figure 3 depicts the biphoton correlations between the signal forward-idler backward (SF-IB) channels. Here, we clearly see a complementary effect compared to Figure 2. Taken together, we understand that as the correlations are diminishing in the copropagating configuration they are intensifying in the counterpropagating configuration, and vice versa. Thus biphoton correlations oscillate between configurations, and an estimate of the modulation period infers that the process originates from a resonance splitting of approximately 1 GHz, which is in good agreement with the measured splitting of the signal and idler resonances.

In Figure 4, we measure the biphoton correlations for the SF-IB configuration using two different values of pump-cavity frequency detuning. Although we are measuring the same channel configuration, we are able to achieve oscillatory features that are completely out of phase with each other. Varying the detuning causes the counterpropagating intracavity pump fields to develop different relative phases (see Figure 1), which may be used to conveniently control the oscillations.

We have shown for the first time that optical microresonators can be used to achieve Rabi-like oscillations in photon pair correlations. We have also demonstrated that the oscillations may be controlled by varying the relative phase of the counterpropagating intracavity pump fields. Given the vital role that second-order coherence assumes in many quantum photonic systems [7], we expect that this new phenomenon will have a broad impact. Photon pairs produced by SFWM are intrinsically time-energy entangled, and we have demonstrated that their correlation properties may be highly coupled to the path configuration of our system. Consequently, we envision that our device may be used to explore quantum state generation and new entanglement properties, as well as the potential for quantum logic operations.

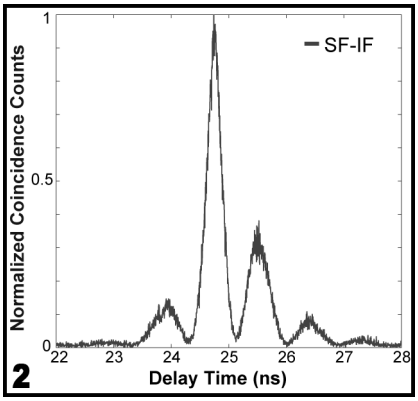

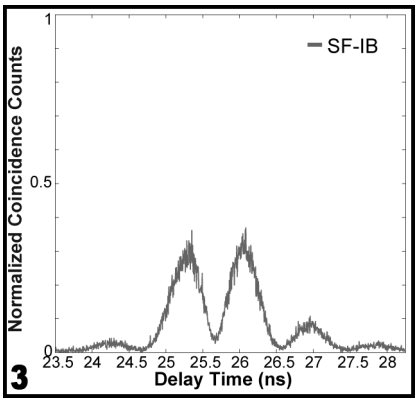

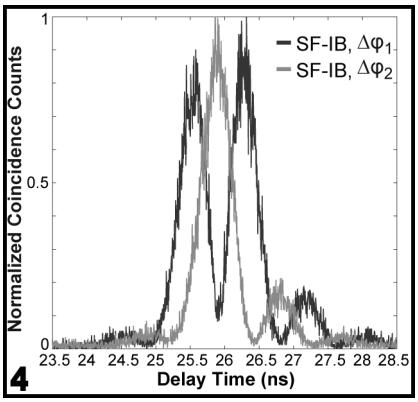

Figure 2, top: Cross-correlation between signal forward (SF) and idler forward (IF). Figure 3, middle: Cross-correlation between signal forward (SF) and idler backward (IB). Figure 4, bottom: Cross-correlation between signal forward (SF) and idler backward (IB), with the black data taken with the counterpropagating intracavity pump modes in phase and the light gray data taken with a relative phase shift of nearly 180 degrees.

References:

[1] D. V. Strekalov, et al. J. Opt. 18, 123002 (2016).

[2] X. Lu, et al. Optica 3, 1331-1338 (2016).

[3] S. Rogers, et al. ACS Photonics 3, 1754-1761 (2016).

[4] D. S. Weiss, et al. Opt. Lett. 20, 1835-1837 (1995).

[5] R. J. Thompson, et al. Phys. Rev. Lett. 68, 1132-1135 (1992).

[6] X. Lu, et al. ACS Photonics 3, 1626-1636 (2016).

[7] J. O'Brien, et al. Nat. Photonics 3, 687-695 (2009).

X-Ray Transmission Optics Development

CNF Project Number: 2172-12

Principal Investigators: Arthur Woll[2], Joel Brock[2,3], Ernie Fontes[2]

User: David Agyeman-Budu[1]

Affiliations: 1. Materials Science and Engineering, 2. Cornell High Energy Synchrotron Source (CHESS), 3. Applied and Engineering Physics; Cornell University

Primary Sources of Research Funding: CHESS is supported by the NSF and NIH/NIGMS via NSF award DMR-1332208

Contact: aw30@cornell.edu, jdb20@cornell.edu, ef11@cornell.edu, da76@cornell.edu

Website: http://www.chess.cornell.edu/

Primary CNF Tools Used: Plasma-Therm deep Si etcher, Xactix XeF_2 etcher

Abstract:

We report the development and performance tests of x-ray transmission mirrors (XTM) fabricated using a new process that is both simpler and has higher yield than prior techniques. The new approach requires only two etch steps, and yet yields more structurally stable devices and accommodates greater versatility for tailoring devices to specific applications. The performance of these devices, namely their transmission and reflection characteristics in the x-ray regime, were tested at the G2 station at the Cornell High Energy Synchrotron Source and agree with theoretical models.

Summary of Research:

X-ray transmission mirrors (XTMs) are a novel class of x-ray optics. As with traditional x-ray mirrors, they operate on the principle of total external reflection (TER): for a given incidence angle, only x-ray energies below a certain critical angle are reflected, so that the mirror acts as a low-pass filter for x-rays. However, unlike a regular x-ray mirror, XTMs transmit the incident x-ray beam rather than absorbing it and can thus act as an efficient high-pass filter. This operating mechanism is illustrated in Figure 1. Because XTMs operate at glancing incident angles, transmitting the incident beam with minimal absorption losses requires XTMs to be designed as thin as possible.

Despite being introduced over 30 years ago [1], XTMs have not been adopted widely in the synchrotron community owing, primarily, to practical challenges of fabricating such optics to be structurally stable. There are many potential applications of XTMs. First, they function as a high-pass x-ray energy filter with sharper energy cut-off and rejection than absorption filters [1,2]. Secondly, together with a total reflection mirror, transmission mirrors can be used as a high flux, tunable x-ray bandwidth optic for applications such as Laue diffraction [3]. They also show promise as a front-end x-ray optic to alleviate the high heat load of a white x-ray beam by reflecting the lower energy components of the spectrum. In this report, we present a new nanofabricated approach developed to fabricate XTMs in a silicon wafer substrate that has resulted in a higher yield of XTIM optics fabricated.

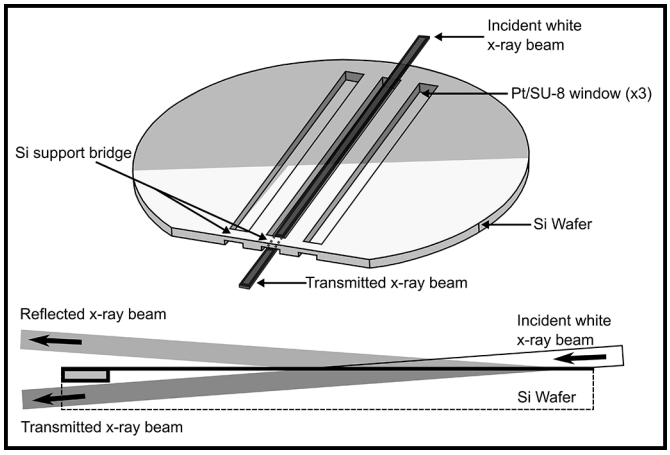

Figure 1: The drawing of a transmission mirror optic showing a 3D representation (top) and a 2D cross-sectional view (bottom) illustrating the mode of operation. By taking advantage of aspect ratio dependent etching (ARDE), a bridge as indicated is created at the downstream of the optic, which functions as the supporting structure for holding up the thin XTM.

Figure 1 shows the principle of operation of an XTM operating at glancing angles. Ideally, the exit path of both the reflected and transmitted beam after interacting with the mirror must be clear. This requirement indicates there should not be any structures at the downstream of wafer in the path where the beam exits the mirror. To avoid blocking the reflected beam, our XTM design was made to support the membrane from the bottom. This support structure was accomplished with a custom

designed etch mask designed to induce a spatial etch rate variation on same wafer using a single deep reactive etch (DRIE) run. In this case, we get to choose which areas of the final optic etches faster and which areas are etched slower.

Starting with a double-side polished silicon wafer, a silicon dioxide etch mask is patterned on the backside to define the eventual support frame of the XTM when the wafer is etched deep. A special, thin formulation of SU-8 (SU-8 TF 6000, ~ 300 nm thick) is spun-on the front side of the wafer. Because the SU-8 film functions as the template membrane for the XTM mirror, care is taken to ramp up the spin speed of the wafer chuck to minimize the overall wafer thickness variation of the SU-8 film. To crosslink the SU-8, a flood exposure on the SÜSS MicroTec MA6 for 4s at a power of 12 mW/cm^2 is enough, which is followed by a 300°C 3hr anneal to relieve any inherent stresses built-up in the SU-8. A 10-nm thick platinum film is sputtered over the SU-8 on the topside of the wafer. The rest of the processing is a deep reactive ion etch (DRIE) on the backside to create the XTM windows after which an isotropic XeF_2 etch finishes off the support bridge structures of the XTM and clears any residual silicon to fully expose the XTM window membranes.

The mirrors were tested at the G2 station at the Cornell High Energy Synchrotron Source (CHESS). The incident beam used was a 0.1 mm tall by 0.5 mm wide x-ray beam. The mirror was then rocked in the beam while the reflection and transmission response was recorded by the MYTHEN single-photon-counting silicon microstrip detector located further downstream of the mirror.

Figure 2 shows the 2D plot of the captured reflection and transmission response for each rotation angle. Integrating the reflected and transmitted beam intensities shows the complementary response function of the mirror which agrees to the predicted behavior as seen in Figure 3.

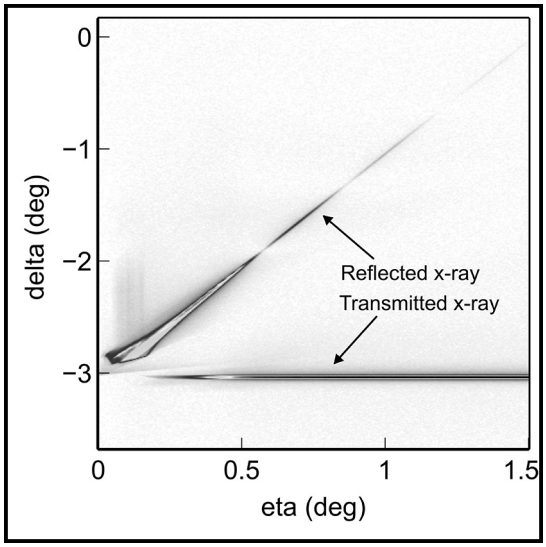

Figure 2: A 2D representation of the reflected and transmitted beam exiting an XTM optic at different incident grazing angles.

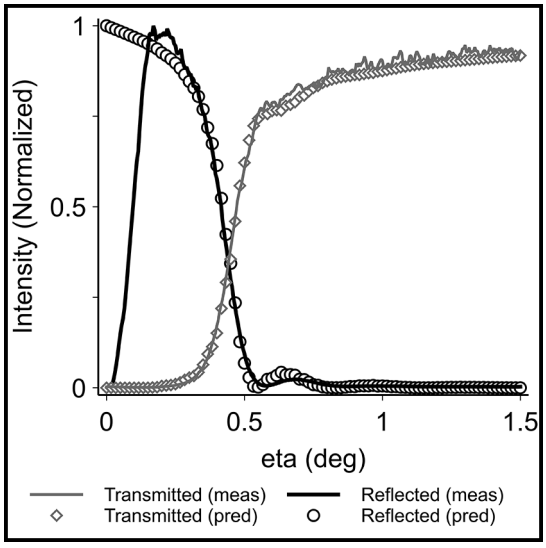

Figure 3: Measured (scaled) and calculated integrated intensities of the reflected and transmitted x-ray beams.

References:

[1] Lairson, B. M., and D. H. Bilderback. "Transmission x-ray mirror -A new optical element." Nuclear Instruments and Methods in Physics Research 195, no. 1-2 (1982): 79-83.

[2] Cornaby, Sterling, and Donald H. Bilderback. "Silicon nitride transmission X-ray mirrors." Journal of synchrotron radiation 15, no. 4 (2008): 371-373.

[3] S. Cornaby, D. M. E. Szebenyi, D.-M. Smilgies, D. J. Schuller, R. Gillilan, Q. Hao and D. H. Bilderback. "Feasibility of one-shot-per-crystal structure determination using Laue diffraction." Acta Crystallographica Section D: Biological Crystallography 66, no. 1(2010): 2-11.

TiO_2 Slot Waveguide for Efficient On-Chip Raman Spectroscopy

CNF Project Number: 2255-13

Principal Investigator: Jin Suntivich[1,2]

User: Chengyu Liu[3]

Affiliations: 1. Materials Science and Engineering Department, 2. Kavli Institute at Cornell for Nanoscale Science, 3. School of Applied and Engineering Physics; Cornell University

Primary Source of Research Funding: Samsung Advanced Institute of Technology (SAIT)

Contact: js2765@cornell.edu, CL986@cornell.edu

Primary CNF Tools Used: PVD75 sputter deposition, AJA sputter deposition, JEOL 9500, PT770 etcher, Oxford 100 etcher

Abstract:

On-chip integrated Raman spectroscopy offers an attractive route to on-chip sensing, owing to its portability and signal enhancement in comparison to conventional Raman spectroscopy [1-3]. In order to further improve the Raman conversion efficiency over the previous work, we design a titanium dioxide (TiO_2) slot waveguide, which has a stronger overlap with the surrounding molecule and a reduced mode volume, which when combined with the high refractive index of TiO_2, allows the theoretical conversion efficiency to be five times higher than strip waveguides. We fabricate the proposed TiO_2 slot waveguides using a combination of e-beam lithography and chromium (Cr) hard mask. The propagation loss is about 15 dB/cm at 780 nm wavelength, which makes this platform promising for the next-generation integrated on-chip Raman sensors.

Summary of Research:

Fully-integrated on-chip Raman sensors are a critically needed technology for medical diagnostics, threat detection, and environmental-quality monitoring. By utilizing a waveguide design using the evanescent field outside of a dielectric to pump and collect Raman scattering, we have demonstrated an integrated-evanescent Raman sensor on TiO_2 [2]. In order to further improve this on-chip Raman sensing platform, we propose a slot waveguide structure that has an air gap between two parallel bus waveguides to improve the Raman efficiency. In this slot waveguide structure, the electric field discontinuity at the TiO_2/air interface leads to a high confinement of the optical field in the slot region, which makes this structure appealing for sensing applications.

We fabricate the proposed TiO_2 slot waveguides using a combination of e-beam lithography and Cr hard mask. The fabrication flow is shown in Figure 1. Since the design slot width is around 100 nm, which is beyond the resolution of conventional photolithography, we switch to e-beam lithography from our previous work [2].

We start with a silicon substrate with thermal oxide on top and sputter TiO_2 thin film using PVD75 deposition tool. Above TiO_2 thin film, we first sputter a thin layer of Cr as a hard mask and then the e-beam resist for e-beam lithography (Figure 1a). After e-beam exposure and development (Figure 1b), we transfer the slot pattern to Cr layer by dry etching in PT770 ICP (Figure 1c). Then we remove the residual e-beam resist by oxygen plasma (Figure 1d) and transfer the slot pattern to TiO_2 layer by dry

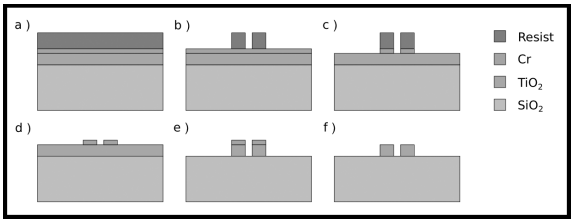

Figure 1: The fabrication process of TiO_2 slot waveguides.

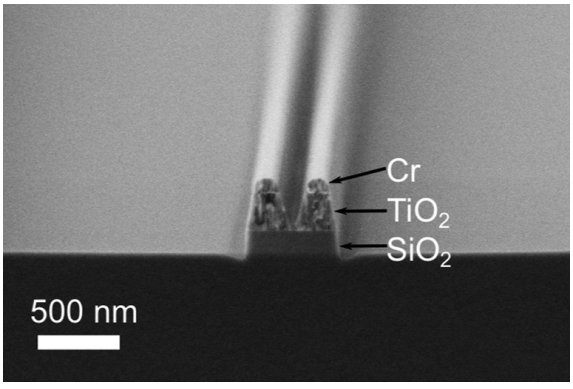

Figure 2: A SEM image of the TiO_2 slot structure after TiO_2 dry etching.

etching in Oxford 100 ICP (Figure 1e). Finally, we remove the Cr hard mask by wet etch (Figure 1f) to form TiO_2 slot waveguides. Figure 2 is a representative scanning electron micrograph (SEM) of the cross section of a fabricated TiO_2 slot waveguide after TiO_2 dry etching step. By utilizing a thin layer of Cr as the hard mask for TiO_2 etch, we are able to define an air gap between two parallel bus waveguides for Raman sensing purpose.

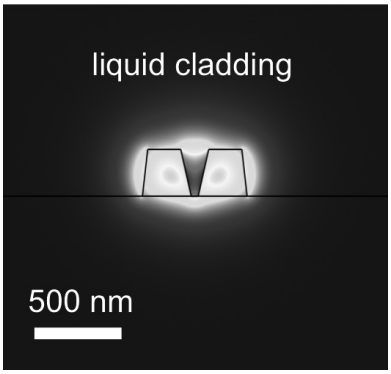

Figure 3: Calculated guiding mode profile of the slot waveguide structure at 780 nm.

In order to characterize this device's performance, we measure the propagation loss using the top-view camera method around 780 nm wavelength in air. We couple a 780 nm laser light into the slot waveguide by an objective lens and capture the waveguide scattering by a camera mounted on the top. We measure the scattering as a function of waveguide length, subtracting the average baseline signal (non-zero dark regions away from the waveguide), and plot the scattering intensity as a function of distance. Then we fit this data to a linear regression model and extract a loss value of about 15 dB/cm. Compared with the previous result by a conformal atomic layer deposition re-coating method to create TiO_2 slot waveguides (767 dB/cm at 664 nm wavelength) [4], our fabrication method has dramatically decreased the device propagation loss, which makes this platform more practical for on-chip Raman sensing application.

We notice that TiO_2 slot etching generates non-vertical sidewalls, so we include those dimension changes and simulate the mode profile in our TiO_2 slot waveguide structure. Figure 3 shows that our fabricated slot structure can support a quasi-TE guiding mode, which is highly confined in the gap region. Based on our previous model of waveguide-based spontaneous Raman scattering conversion efficiency η_0 [2], η_0 is related to the overlap between guiding light and sensing chemistry. This quasi-TE mode in the slot structure has a stronger overlap with the surrounding molecule than that in strip waveguides, which makes the slot waveguide structure more in favor of Raman sensing than a strip waveguide structure. Our calculation reveals that our TiO_2 slot waveguide design has a five-fold η_0 than optimized strip waveguides that were made of TiO_2 as well.

In conclusion, we propose a slot structure on TiO_2 integrated optics platform for efficient on-chip Raman sensing. We fabricate TiO_2 slot waveguides and the low loss (15 dB/cm) of our TiO_2 waveguide puts it as one of the best performing slot waveguide. Future work will focus on the control of the fabrication variation and repeatability and the demonstration of high-performance sensing.

References:

[1] Dhakal, A., Subramanian, A. Z., Wuytens, P., Peyskens, F., Le Thomas, N., and Baets, R. (2014). Evanescent excitation and collection of spontaneous Raman spectra using silicon nitride nanophotonic waveguides. Optics letters, 39(13), 4025-4028.

[2] Evans, C. C., Liu, C., and Suntivich, J. (2016). TiO_2 Nanophotonic sensors for efficient integrated evanescent Raman spectroscopy. ACS Photonics, 3(9), 1662-1669.

[3] Dhakal, A., Wuytens, P., Peyskens, F., Subramanian, A., Skirtach, A., Le Thomas, N., and Baets, R. (2015, May). Nanophotonic lab-on-a-chip Raman sensors: A sensitivity comparison with confocal Raman microscope. In BioPhotonics (BioPhotonics), 2015 International Conference on (pp. 1-4). IEEE.

[4] Häyrinen, M., Roussey, M., Säynätjoki, A., Kuittinen, M., and Honkanen, S. (2015, February). Slot waveguide ring resonators for visible wavelengths in ALD titanium dioxide. In Integrated Optics: Devices, Materials, and Technologies XIX (Vol. 9365, p. 936513). International Society for Optics and Photonics.

Developing Full Wafer Blazed Grating Fabrication Method Using Stepper

CNF Project Number: 2292-14

Principal Investigator: Cori Bargmann

Users: Sara Abrahamsson, Philip Kidd

Affiliation: Lulu and Anthony Wang Laboratory for Neural Circuits and Behavior, Rockefeller University, NYC NY

Primary Source of Research Funding: Lab funds

Contact: cori.bargmann@rockefeller.edu, sara.abrahamsson@gmail.com

Primary CNF Tools Used: ASML stepper, Heidelberg DWL2000 Laserwriter, Oxford 80 etcher, AFM, Hamatech wafer processing tools

Summary of Research:

With the help of John Treichler and Garry Bordonaro we were able to devise a method to print a blazed grating on an entire 100 mm fused silica ("glass") wafer, and to cut out four standard 29 mm circular filter size pieces from each wafer. These diffractive optical components will be used as a chromatic correction element in a multi-camera microscopy system for 3D imaging of neural circuits.

512-Element Actively Steered Silicon Phased Array for Low-Power LIDAR

CNF Project Number: 2364-15

Principal Investigator: Michal Lipson

Users: Steven A. Miller, Christopher T. Phare, You-Chia Chang, Xingchen Ji, Oscar A. Jimenez Gordillo, Aseema Mohanty, Samantha P. Roberts, Min Chul Shin, Brian Stern, Moshe Zadka

Affiliation: Department of Electrical Engineering, Columbia University, New York, NY 10027

Primary Source of Research Funding: DARPA

Contact: ML3745@columbia.edu, spr2127@columbia.edu

Website: lipson.ee.columbia.edu

Primary CNF Tools Used: BOSCH etcher, AJA sputter deposition, CVC sputter deposition, Cu electroplating tanks, Oxford 100 ICP RIE

Abstract:

Solid-state beam steering using large-scale optical phased arrays is of great interest for LIDAR and free-space communication systems, enabling wide-angle, long distance ranging or transmission of data in a robust platform. Ideally, a widely steerable narrow output beam that can reach to long distances requires a large aperture containing a large number of independently phase-controlled elements while remaining at a reasonable total power consumption. Applications at distances of tens to hundreds of meters require element-counts of several thousands, such that independent phase control overwhelmingly dominates power consumption and has prohibited larger element-count demonstrations thus far. We demonstrate the highest yet-reported element count actively-steered optical phased array with record low array power consumption of < 1.8 W. We show 2D steering over a 70 × 14° field of view while pumped by an integrated InP/silicon laser.

Summary of Research:

Here, we demonstrate low-power 2D beam steering with a 512-element active silicon optical phased array—to our knowledge the largest independently controllable phased array to date. We achieve low power operation by using a resonance-free light recycling device to re-circulate light multiple times through a single thermo-optic phase shifter, thus multiplying its efficiency by approximately the number of circulations [1]. We place a 5-pass light recycling structure on every element (Figure 1b). Phase shifter power and voltage is sufficiently low to be directly driven by off-the-shelf digital to analog converter integrated circuits. The input laser light is split in a binary splitter tree into 512 channels, each of which then have a high-efficiency thermo-optic phase-shifter. The phase-shifters are separated by 20 μm to minimize thermal crosstalk, and are then fanned-in to a 1.3 μm emitter spacing.

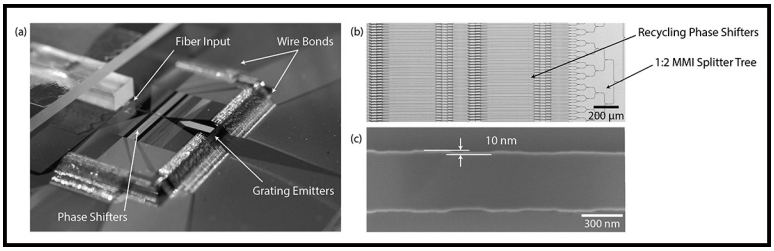

Figure 1: (a) 512-element silicon photonic array chip wire-bonded to interposer. (b) Microscope image of a section of the array of recycling phase shifters and tree of 1:2 MMI splitters (light flows right to left). (c) Scanning electron micrograph of sidewall grating on 450 nm wide emitter waveguide.

Finally, a 1D array of 1-mm-long sidewall gratings [shown in Figure 1(c)] direct the beam upwards out of the chip and allow for 2D beam steering via wavelength tuning of our integrated laser in the vertical direction due to the 0.3°/nm wavelength sensitivity of the grating emission. Two layers of aluminum metal on the photonic chip route signals and a common ground to peripheral bond pads, where they are attached to a single layer of aluminum on a silicon interposer. The interposer is then mounted and wire bonded to a standard printed circuit board and its wires routed to control circuitry. The packaged chip is shown in Figure 1(a).

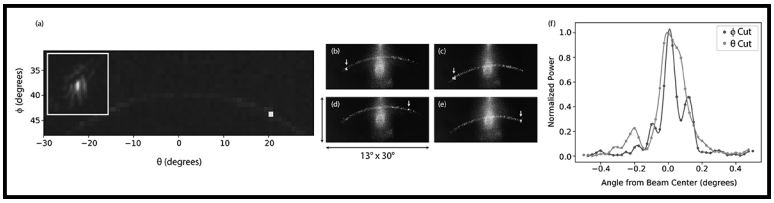

Figure 2: Measured far-field optical power for a beam steered 20° off-axis in the phase-tuned direction. (a) Widefield scan showing beam at 20° off axis. Faint arc is residual power confined by the grating, but not completely confined by the phased array. Inset is a detail 2° × 2° view of the beam. (b-e) Fourier-plane camera images of beams pointed to θ, ϕ *of (b) -20°, 42°, (c) -20°, 48°, (d) +20°, 42°, (e) +20°, 48°. Sidelobe power is exaggerated due to limited camera dynamic range. (f) Cuts in* ϕ *and* θ *axes through the center of the beam in (a).*

For our laser source, we fabricate an external laser cavity in silicon using vernier ring filters and couple it to an off-the-shelf facet-emitting reflective semiconductor optical amplifier (RSOA). This compact integrated laser source is both broadly tunable over tens of nanometers, while exhibiting sub-MHz narrow linewidth. For this demonstration light is coupled between separate laser and phased array chips with a single mode optical fiber.

We show a 2D-steerable phased array with a beam width of ~ 0.15° in both axes. To converge a single beam for each angle in the 2D phi-theta space and to compensate for as-fabricated phase mismatch between channels, we use a single-element photodiode placed physically in the far-field and a global optimization algorithm [3]. A far-field scan of the beam is shown Figure 2(a) as well as a fine scan in Figures 2(b) and 2(c), showing a peak-to-sidelobe ratio of 8.0 dB. Beam divergence and peak-to-sidelobe in the phase-controlled axis are slightly diminished from the theoretical values of 0.13° and 13 dB due to low phase shifter yield (63%) from a metal-layer fabrication error. The beam width of 0.15° in the grating axis confirms an effective grating length of approximately 1 mm. We demonstrate 2D beam steering of ± 35° in the phase-tuned axis (ϕ in Figure 2) and a ± 7° in the wavelength tuned axis (θ in Figure 2) grating axis by tuning the laser bandwidth over a 45 nm (controlled by microheaters on the vernier ring filters). For accessing any steering point, the phased array consumes 1.5-1.8 W.

This large size array is already adequate for application around 10m operation for ranging or communication applications. Further optimization of our beam-forming algorithm coupled with improved phase-shifter efficiency and additional phase re-circulation can yield several factors improvement to scale up toward hundreds of meters. Considering that the laser efficiency is on the order of 4% [2], for input laser light of 50 mW (corresponding to the maximum output power of typical RSOAs), we estimate total power consumption less than 3W, enabling the array to be operated by a compact battery pack.

References:

[1] You-Chia Chang, Samantha P. Roberts, Brian Stern, and Michal Lipson, "Resonance-Free Light Recycling." arXiv:1710.02891 (2017).

[2] Brian Stern, Xingchen Ji, Avik Dutt, and Michal Lipson, "Compact narrow-linewidth integrated laser based on a low-loss silicon nitride ring resonator." Opt. Letters 42, 4541-4544 (2017).

[3] Christopher T. Phare, Min Chul Shin, Steven A. Miller, Brian Stern, and Michal Lipson, "Silicon Optical Phased Array with High-Efficiency Beam Formation over 180 Degree Field of View." arXiv:1802.04624 (2018).

Wide Bandgap Semiconductor Deep UV Devices

CNF Project Number: 2387-15

Principal Investigator: Debdeep Jena

Users: Kevin Lee, Shyam Bharadwaj

Affiliation: School of Electrical and Computer Engineering, Cornell University

Primary Source of Research Funding: Designing Materials to Revolutionize and Engineer our Future, E70-8276

Contact: djena@cornell.edu, KL833@cornell.edu, sb2347@cornell.edu

Website: https://sites.google.com/a/cornell.edu/photonic-devices/home

Primary CNF Tools Used: Veeco Icon atomic force microscope, ABM contact aligner, photolithography tools (spinners, hot plates, solvent hoods), SC4500 e-beam evaporators, AG610 RTA, PT770 ICP etcher, YES Asher, Oxford 81 RIE, profilometers, Filmetrics

Abstract:

Our main research goal is to improve and fabricate deep UV and visible photonic devices (e.g., LEDs and lasers). We grow the semiconductor thin films by molecular beam epitaxy. We use III-Nitride materials to make such devices. For deep UV devices, wide bandgap materials such as AlN, GaN and AlGaN are the typical materials. *P*-type transport is a major challenge in UV-LEDs. As such, we are working on polarization induced and short period superlattice doping to enhance the active hole concentration in these devices. For visible LEDs, we use tunnel junctions to improve the current spreading and contact resistance.

Summary of Research:

We have grown high aluminum (Al)-content *p*-type transport layers by plasma-assisted molecular beam epitaxy (PA-MBE). These transport layers are grown on MOCVD-grown AlN on sapphire template. Using polarization induced doping, we grew magnesium (Mg)-doped graded AlGaN layers (grading from 100% Al-content to 65%). We also grew Mg-doped AlGaN/AlN short period superlattice structures to compare their performance. AFM images taken in CNF and XRD characterizations are shown in Figure 1.

We used standard lithography tools in CNF to fabricate transmission line measurement (TLM) structures on the *p*-type transport layers. Due to large resistivity in these *p*-type transport layers, we were not able to perform Hall measurements. Therefore, we performed temperature dependent TLM to extract the resistivity of our films and activation energy of the Mg dopant. As shown in Figure 2, the graded *p*-AlGaN structure has improved resistivity over the standard constant *p*-AlGaN structures. These results have been presented in the 2017 international workshop in UV materials and devices in Japan.

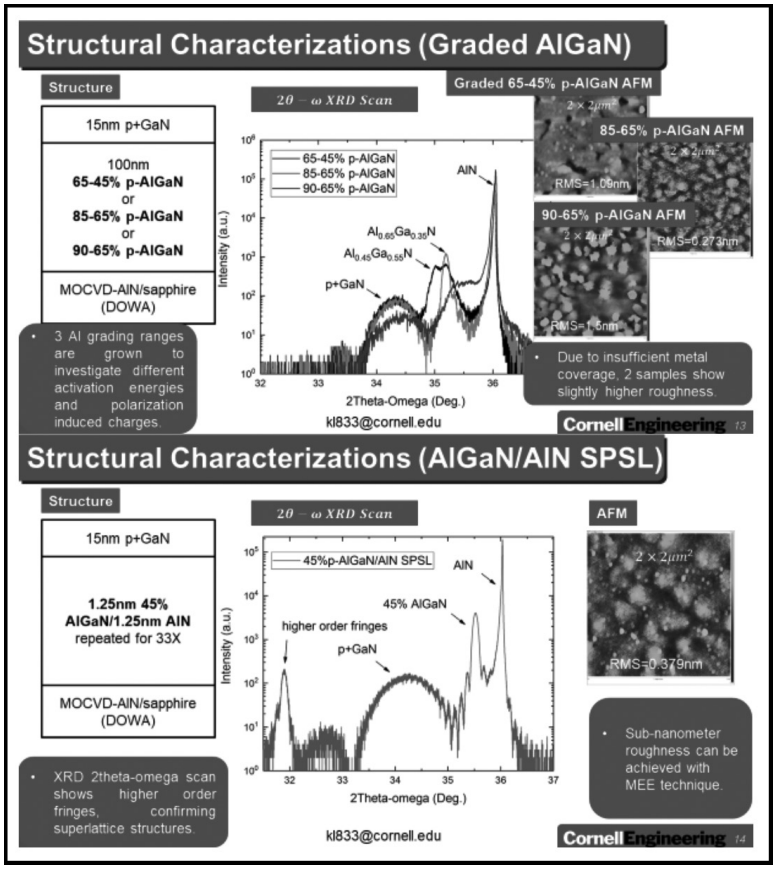

Figure 1: AFMs of grown p*-type transport layers on AlN/sapphire substrate.*

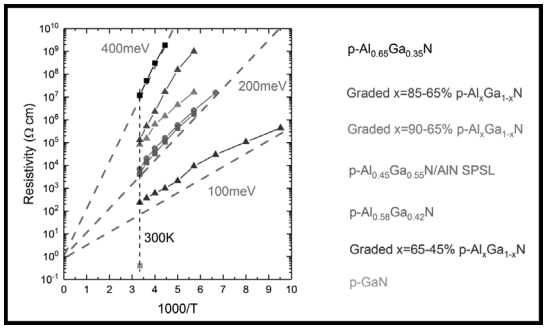

Figure 2, above: Temperature dependent TLM showed two orders less resistivity for graded AlGaN structure over constant AlGaN.

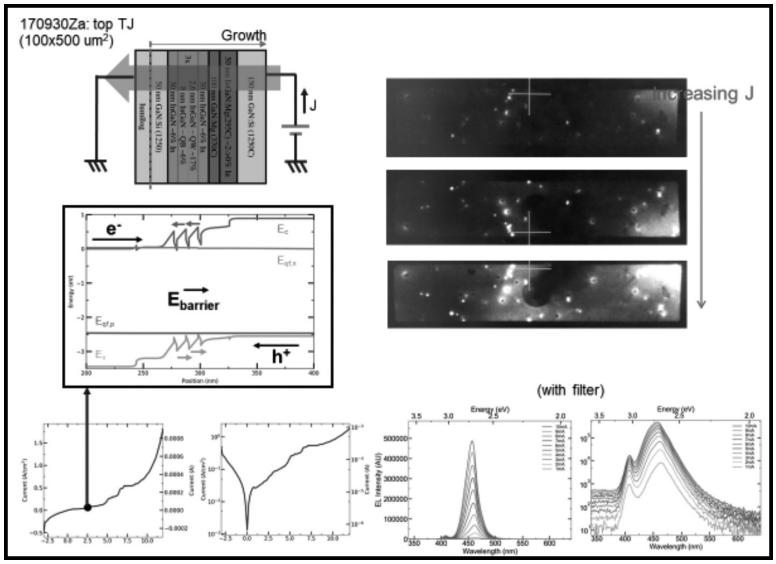

Figure 3, right: Summary of top tunnel junction (TJ) structure's J-V curves and electroluminescence spectrum.

Another approach to resolve the resistive *p*-type layer issue in nitrides is to use tunnel junction. Using tunnel junction, instead of using top *p*-type layer, we grew another *n*-type layer on top of *p*-layer to form a tunnel junction. This is so called top tunnel junction design. Using this strategy, it has two advantages. First, due to low resistivity in *n*-type layer, the current spreading is generally three orders better. Second, making contact to the *n*-layers is also much easier, meaning lower contact resistance.

We grew these structures on single crystal bulk gallium nitride (GaN) substrates. And we used the standard lithography tools to do MESA isolation and put down the contacts. We've successfully demonstrated both top tunnel junction blue LEDs operating at room temperature as shown in Figure 3. The next step will be measuring these devices' external quantum efficiency and output power to benchmark them with respect to other methods.

Three-Dimensional Scanner Fabrication

CNF Project Number: 2406-15
Principal Investigator: David L. Dickensheets
User: Tianbo Liu

Affiliation: Electrical and Computer Engineering Department, Montana State University
Primary Source of Research Funding: National Institutes of Health
Contact: davidd@montana.edu, tianbo.liu@msu.montana.edu
Website: http://www.montana.edu/ddickensheets/
Primary CNF Tools Used: Photolithography, plasma etching, electron beam evaporation wet chemical processing

Abstract:

A three-dimensional (3D) micro-electromechanical scanner that is capable of providing biaxial scanning and focus control is constructed. The scanner serves as the optical engine in a miniaturized handheld confocal microscope for the non-invasive, *in vivo* detection of skin cancer.

Introduction:

The standard method of diagnosing suspicious growths on the skin is to perform a biopsy. However not only can biopsies be painful and cause permanent scarring, they are also a sparse sampling [1,2]. It would be impractical to prescribe a biopsy for each site that looks suspicious, which leaves room for some malignant cells to go unnoticed. The good news is that a new, non-invasive method called optical biopsy is on the horizon. One of the promising types of optical biopsy is confocal laser scanning microscopy, which uses a laser to image cells under the surface of the skin [3,4]. The problem is that current confocal microscopes are too big, making it difficult to image sites that are in hard-to-reach parts of the body. A microelectromechanical system (MEMS) scanner has been constructed to address this problem by replacing the cumbersome mechanical scanning and focus elements in the conventional confocal microscope with a single 10 mm device [5,6].

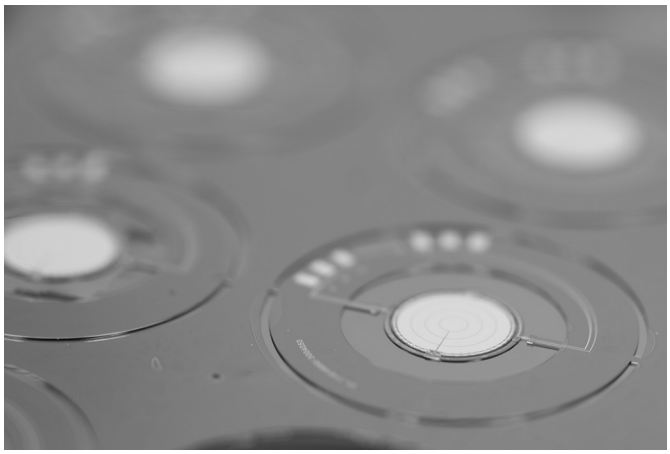

Figure 1: Image of wafer after fabrication. See the full color version on the cover of this book!

Summary of Research:

The device is based on a dual axis gimbal platform that is supported by polymer hinges over a set of quadrant electrodes. At the center of the dual-axis gimbal platform is a deformable mirror that can be actuated independently using its own set of concentric electrodes. The gimbal platform along with a deformable mirror is constructed using a silicon-on-insulator (SOI) wafer, while the quadrant electrodes for scanning actuation are fabricated on a double-sided polished (DSP) silicon wafer. The fabrication process includes the making of the deformable structure, the optical surface, the electrical connections and the polymer hinges. These are completed using microfabrication techniques such as photolithography, plasma etching, electron beam evaporation and wet chemical processing. The quadrant electrodes on the DSP wafer are fabricated using similar techniques. The two wafers are then aligned and bonded.

The release of the device uses procedures including xenon difluoride etching with the Xactix etcher to remove the device layer silicon from the SOI. Low power oxide etching employing the Oxford 81 etcher is used to remove the buried oxide layer. Figure 1 provides a picture of the completed wafer.

Conclusions:

In conclusion, we have fabricated a new polymer enhanced MEMS scan mirror that is capable of high-resolution imaging with simultaneous focus adjustment. The device is geared towards the miniaturization of confocal microscopes for a new generation of handheld optical biopsy devices. It can also be adapted to benefit a wide range of optical imaging and display applications.

References:

[1] G. Argenziano, et al., Accuracy in melanoma detection: a 10-year multicenter survey," Journal of the American Academy of Dermatology, vol. 67, no. 1, pp. 54-59. e1, 2012.

[2] I. Kovalyshyn, S. W. Dusza, K. Siamas, A. C. Halpern, G. Argenziano, and A. A. Marghoob, "The impact of physician screening on melanoma detection," Archives of dermatology, vol. 147, no. 11, pp. 1269l-1275, 2011.

[3] A. Gerger, et al., "*In vivo* confocal laser scanning microscopy of melanocytic skin tumours: diagnostic applicability using unselected tumour images," British Journal of Dermatology, vol. 158, no. 2, pp. 329-333, 2008.

[4] P. Guitera, et al., "The impact of *in vivo* reflectance confocal microscopy on the diagnostic accuracy of lentigo maligna and equivocal pigmented and nonpigmented macules of the face," Journal of Investigative Dermatology, vol. 130, no. 8, pp. 2080-2091, 2010.

[5] T. Liu and D. L. Dickensheets, "Three-Dimensional beam scanner for a handheld confocal dermoscope," in Optical MEMS and Nanophotonics (OMN), 2016 International Conference on, 2016, pp. 1-2: IEEE.

[6] T. Liu and D. L. Dickensheets, "MEMS 3-dimensional scanner for handheld confocal microscope," in Optical MEMS and Nanophotonics (OMN), 2017 International Conference on, 2017, pp. 1-2: IEEE.

Development of Single and Double Layer Anti-Reflective Coatings for Astronomical Instruments

CNF Project Number: 2458-16

Principal Investigator: Gordon Stacey[1]

Users: Nicholas Cothard[2], Kenny Vetter[3], Mahiro Abe[3]

Affiliation(s): 1. Department of Astronomy, 2. Department of Applied and Engineering Physics, 3. Department of Physics; Cornell University

Primary Source of Research Funding: NASA Grant NNX16AC72G

Contact: stacey@cornell.edu, nc467@cornell.edu, kjv35@cornell.edu, ma797@cornell.edu

Primary CNF Tools Used: FilMetrics F50-EXR, FleXus film stress measurement, Zygo optical profilometer, ABM contact aligner, ASML 300C DUV stepper, Heidelberg DWL2000, Oxford PECVD, Anatech resist strip, Oxford 82 etcher, Unaxis 770 deep Si etcher

Abstract:

We are developing wide-bandwidth silicon substrate-based metal mesh mirrors for use in millimeter and sub-millimeter astronomical instruments. These mirrors are comprised of silicon substrates that are lithographically patterned with metal mesh reflectors on one surface and metamaterial anti-reflection coatings on their other surface. In the past year, this project has made significant progress in the development of our fabrication methods. We use standard lift-off lithography and metal evaporation tools to deposit and pattern our metal mesh filters. Our two-layer metamaterial anti-reflection coating fabrication makes extensive use of CNF's deep reactive ion etching devices and metrology tools such as profilometry and scanning electron microscopes. We are currently fabricating our meshes and anti-reflection coatings on high-resistivity silicon wafers that are low-loss, optical quality substrates. We will test the optical performance of our samples this summer using a Fourier transform spectrometer and will use the results to iterate and improve on our fabrication processes in the coming year.

Summary of Research:

The goal for this project is to fabricate silicon-substrate based metal mesh filters for use in millimeter and submillimeter astronomical instruments. This involves lithographic patterning of evaporated gold meshes on silicon wafers and etching double-layer metamaterial anti-reflection coatings (ARC) on the silicon surfaces using deep reactive ion etching (DRIE). These frequency dependent filters will be used as mirrors for Fabry-Perot interferometers (FPIs) to spectroscopically observe early star and galaxy formation. The double-layer design is necessary to provide wide bandwidth transmission to span the wavelengths of interest for our instruments. The metamaterial design is necessary to match the thermal expansion coefficients of the substrate and ARC layers because warpage due to cryogenic thin film stresses would strongly affect the optical performance of our interferometry and refractive optical elements.

The bulk of our work this year has been the development of our fabrication methods for high-throughput, wide-bandwidth double-layer metamaterial ARCs. This has involved many iterations of fabrication and metrology with a plethora of tools in the CNF cleanroom. We began investigating the methods to fabricate two-layer ARCs over a year ago and presented preliminary results in an Applied Optics paper last year [1]. Since this time, we have worked to improve our control of the etched geometry. Figure 1 shows our current fabrication recipe for two-layer ARCs.

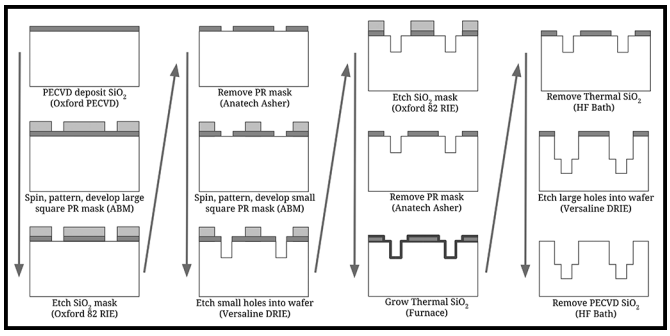

Figure 1: Process flow for fabricating a double-layer ARC on a silicon wafer. Dark grey represents thermal oxide. Light grey represents photoresist. White represents the silicon wafer.

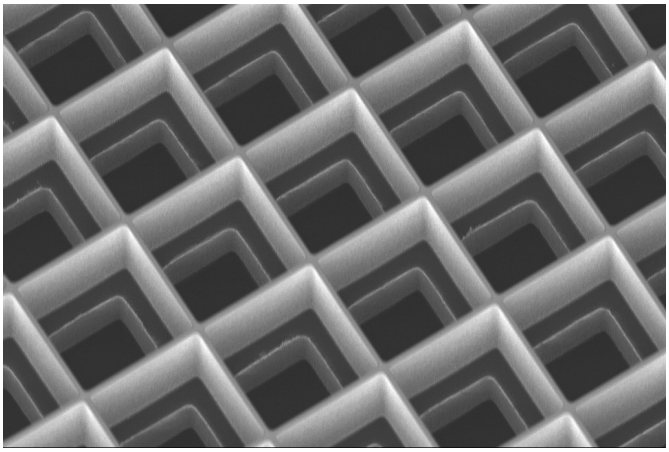

Figure 2: SEM image taken using CNF's Zeiss Ultra SEM showing successful fabrication of our two-layer metamaterial silicon ARC.

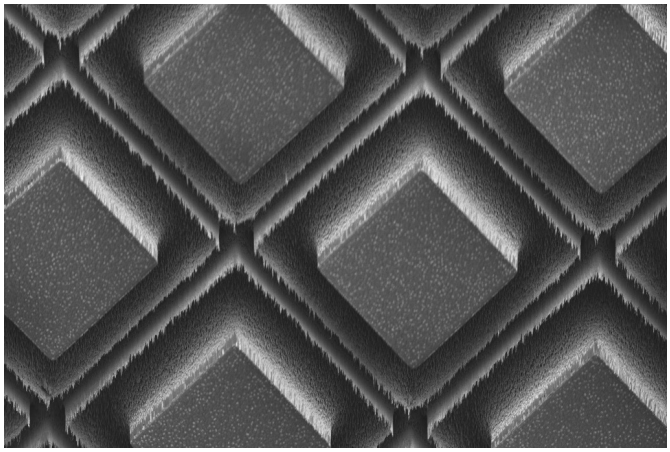

Figure 3: SEM image taken using CNF's Zeiss Ultra SEM showing a two-layer metamaterial silicon ARC with unwanted fence-like features between the upper and lower layers of the ARC.

We use stacked oxide and photoresist etch masks that are patterned on a silicon wafer before any silicon is etched. The oxide is deposited using CNF's Oxford plasma enhanced chemical vapor deposition (PECVD) and etched using the Oxford 82 etcher. Depending on the millimeter or sub-millimeter band that we are interested in, we pattern our photoresist etch masks using the ABM contact aligner or the ASML stepper with Gamma automatic coat-develop tool. With these etch masks patterned, we use either the Unaxis 770 deep silicon etcher or the Plasma-Therm deep silicon etcher. At intermediate steps inside our silicon etching, we measure the etch depth using the Zygo optical profilometer. Since last year, we have added a thermal oxide growth step and oxide removal step in between etching both silicon layers in order to clean-up the edge between both layers.

Figure 2 shows an SEM image (taken using CNF's Zeiss Ultra SEM) of a successful result of this fabrication procedure. Figure 3 shows an SEM image of the result of our old recipe, which did not include the thermal oxidation and HF bath in between the two etched layers. Notice the fence-like structure in between the upper and lower holes. Our new oxidation and removal steps can remove this unwanted structure. We are currently working to improve our control of this method and we are also looking for other methods to prevent the formation of this structure.

We are also currently fabricating these ARCs on optical quality, high-resistivity silicon wafers so that we can measure their transmittance using our lab's Fourier transform spectrometer (FTS) We have also been learning how to use negative lift-off photoresist techniques to pattern metal meshes onto silicon wafers. We have had success doing this using AZ nLOF 2020 photoresist with Microposit 1165 Remover with gold deposition using the CHA evaporator. We are beginning to fabricate these meshes on optical quality silicon so that we can measure their frequency dependent transmittance using our lab's FTS. This summer, we will fabricate meshes of various geometries and compare to our optical models.

These mesh filters and ARCs will be used to fabricate the mirrors of astronomical FPIs, which will be used for spectroscopic measurements in two major instruments. The first will be the HIRMES (high-resolution mid-infrared spectrometer) instrument, which will fly on NASA's airborne observatory Stratospheric Observatory for Infrared Astronomy (SOFIA) [2]. The second will be the CCAT-Prime telescope which Cornell is building on Cerro Chajnantor in the Chilean Atacama Desert [3]. HIRMES will observe in the far-IR, while CCAT-Prime will observe in the millimeter and sub-millimeter. Two wafers with ARC on one side and a metalized layer on the other side will form the resonant cavity of a FPI.

In the past year we have made great steps towards achieving our goals at CNF. We have demonstrated our ability to fabricate double-layer ARCs for different millimeter, sub-millimeter and far-IR wavelengths. We have used many of the fabrication and metrology tools at CNF. Our next steps are to better characterize our etched geometries and improve our metamaterial ARCs. We will be using Fourier transform spectrometers to measure our samples' optical performance and using the results to iterate on our fabrication design.

References:

[1] P.A. Gallardo, B.J. Koopman, N.F. Cothard, S.M.M. Bruno, G. Cortes-Medellin, G. Marchetti, K.H. Miller, B. Mockler, M.D. Niemack, G. Stacey, and E.J. Wollack, "Deep reactive ion etched anti-reflection coatings for sub-millimeter silicon optics," Appl. Opt. 56, 2796-2803 (2017)

[2] https://www.nasa.gov/feature/nasa-selects-next-generation-spectrometer-for-sofia-flying-observatory

[3] http://www.ccatobservatory.org/

Large Area Electrically Tunable Metalens

CNF Project Number: 2471-16

Principal Investigator: Professor Federico Capasso

Users: Alan She, Shuyan Zhang

Affiliation: John A. Paulson School of Engineering and Applied Sciences, Harvard University

Primary Source of Research Funding: Air Force Office of Scientific Research

Contact: capasso@seas.harvard.edu, alan.she@post.harvard.edu, shuyanzhang@seas.harvard.edu

Website: https://www.seas.harvard.edu/capasso

Primary CNF Tools Used: Heidelberg DWL2000, ASML DUV stepper, Gamma auto-coater, CVC sputterer, Oxford 81, 82, and 100 etchers

Abstract:

Our tunable optics technology enables dynamic tuning of metalenses with voltage-resolved precision. We have demonstrated electrically controlled focal length tuning of over 100% as well as the capability of adjusting for astigmatism and image shift at the same time. We have also developed a method for designing and fabricating metalenses of large areas: two-centimeters in diameter and beyond.

Summary of Research:

Large Area Metalenses [1]. Optical components, such as lenses, have traditionally been made in the bulk form by shaping glass or other transparent materials. Recent advances in metasurfaces provide a new basis for recasting optical components into thin, planar elements, having similar or better performance using arrays of subwavelength-spaced optical phase-shifters. The technology required to mass produce them dates back to the mid-1990s, when the feature sizes of semiconductor manufacturing became considerably denser than the wavelength of light, advancing in stride with Moore's law. This provides the possibility of unifying two industries: semiconductor manufacturing and lens-making, whereby the same technology used to make computer chips is used to make optical components, such as lenses, based on metasurfaces. Using a scalable metasurface layout compression algorithm that exponentially reduces design file sizes (by three orders of magnitude for a centimeter diameter lens) and stepper photolithography, we show the design and fabrication of metasurface lenses (metalenses) with extremely large areas, up to centimeters in diameter and beyond. Using a single two-centimeter diameter near-infrared metalens less than a micron-thick fabricated in this way, we experimentally implement the ideal thin lens equation, while demonstrating high-quality imaging and diffraction-limited focusing.

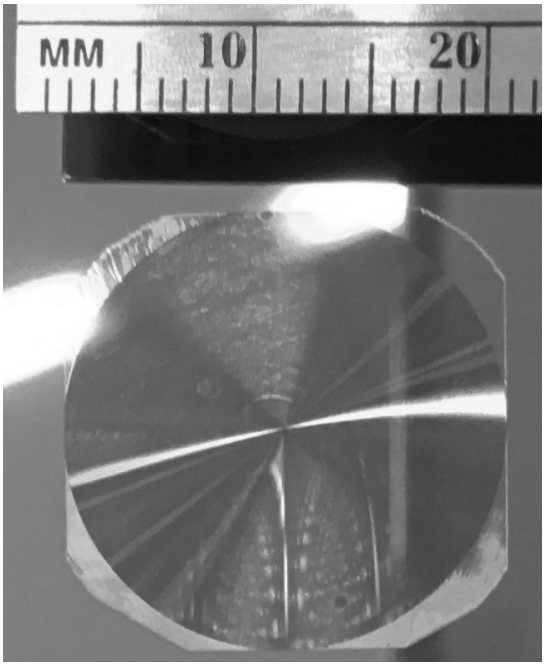

Figure 1: Our metasurface lens with diameter of 2 cm.

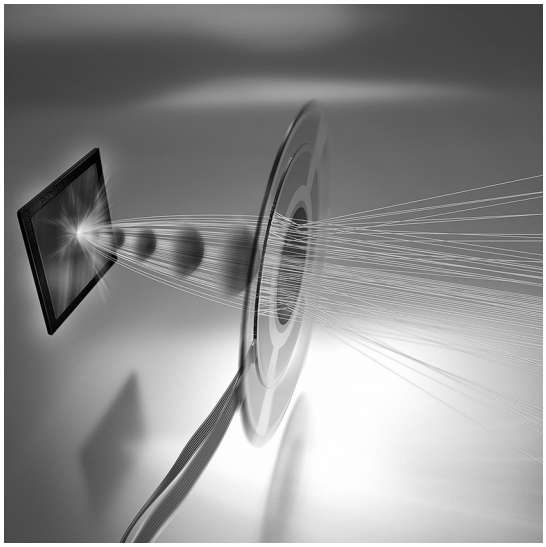

Figure 2: Schematic operation of adaptive metalens, which can perform simultaneous electrical adjustment of focal length, astigmatism, and image shift.

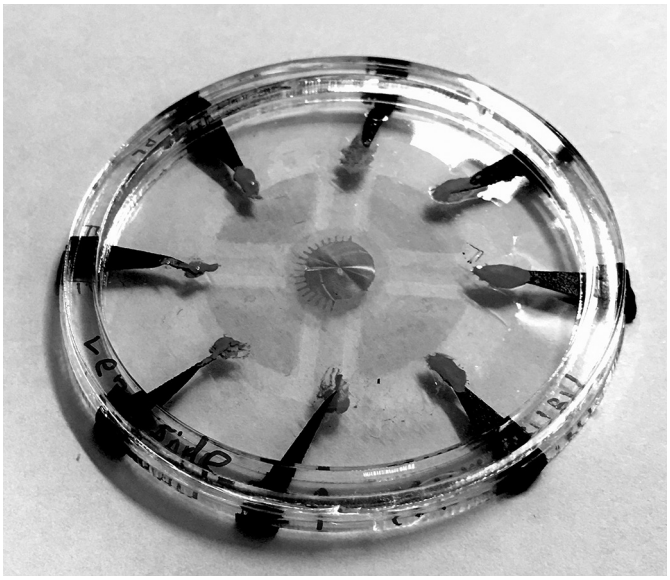

Figure 3: Photo of adaptive metalens device.

Adaptive Metalenses [2]. Focal adjustment and zooming are universal features of cameras and advanced optical systems. Such tuning is usually performed longitudinally along the optical axis by mechanical or electrical control of focal length. However, the recent advent of ultrathin planar lenses based on metasurfaces (metalenses), which opens the door to future drastic miniaturization of mobile devices such as cell phones and wearable displays, mandates fundamentally different forms of tuning based on lateral motion rather than longitudinal motion. Theory shows that the strain field of a metalens substrate can be directly mapped into the outgoing optical wavefront to achieve large diffraction-limited focal length tuning and control of aberrations. We demonstrate electrically tunable large-area metalenses controlled by artificial muscles capable of simultaneously performing focal length tuning (>100%) as well as on-the-fly astigmatism and image shift corrections, which until now were only possible in electron optics. The device thickness is only 30 μm.

Our results demonstrate the possibility of future optical microscopes that fully operate electronically, as well as compact optical systems that use the principles of adaptive optics to correct many orders of aberrations simultaneously.

References:

[1] A. She, S. Zhang, S. Shian, D.R. Clarke, and F. Capasso, "Large area metalenses: design, characterization, and mass manufacturing," Opt. Express 26, 1573-1585 (2018).

[2] A. She, S. Zhang, S. Shian, D.R. Clarke, and F. Capasso. 2018. "Adaptive metalenses with simultaneous electrical control of focal length, astigmatism, and shift." Science Advances 4 (2): eaap9957. doi:10.1126/sciadv.aap9957. http://dx.doi.org/10.1126/sciadv.aap9957.

Multi-Resonant Bianisotropic Metagratings for Ultra-Efficient Diffraction of Mid-Infrared Light

CNF Project Number: 2472-16

Principal Investigator: Gennady Shvets

User: Maxim Shcherbakov

Affiliation: School of Applied and Engineering Physics, Cornell University

Primary Source of Research Funding: ONR grant #N00014-17-1-2161

Contact: gs656@cornell.edu, mrs356@cornell.edu

Primary CNF Tools Used: JEOL 9500, even-hour evaporator, Oxford Cobra

Abstract:

We demonstrate that a bianisotropic metamaterial supporting four optical resonances of the appropriate symmetry can be used as a building block for achieving perfect diffraction of mid-infrared radiation. We design and experimentally realize such bianisotropic metamaterials. We show that near-perfect diffraction to the $^{+}1^{st}$ diffraction order is possible, while other orders are suppressed, in the mid-infrared spectral region.

Summary of Research:

We experimentally verify the viability of the "perfectly" diffracting metagrating in the mid-IR spectral region [1]. The geometric dimensions of the designed structure and corresponding diffraction spectra have been simulated using a finite-element-method software. An undoped, double-side-polished wafer (Ultrasil, Inc.) with a device layer of 2.7 μm and a buried oxide layer of 1.0 μm was cleaned in acetone and isopropyl alcohol (IPA) and coated with two layers of positive electron beam resist: 100 nm of PMMA 950 on top of the 200 nm of PMMA 495k, baking the resist at 170°C for 15 min after each coating step. The desired pattern was exposed over the substrate at 1000 μC/cm^2 (JEOL 9500FS) and developed in MIBK:IPA 1:3 solution for 75 sec, with consequent rinsing in IPA. A 60-nm-thick Cr hard mask was deposited using electron beam evaporator at a rate of 3 nm/min. After liftoff in sonicated acetone (60 sec), HBr plasma dry etching of silicon down to the 1-μm-thick buried oxide layer was carried out (Oxford Cobra), leaving the desired pattern carved in the device layer. As the last step, the residual Cr mask was removed with a Cr wet etch. The patterned area of each metagrating was (1.5 mm)^2. A scanning electron microscope image of the best-performance sample is given in Fig.1(a).

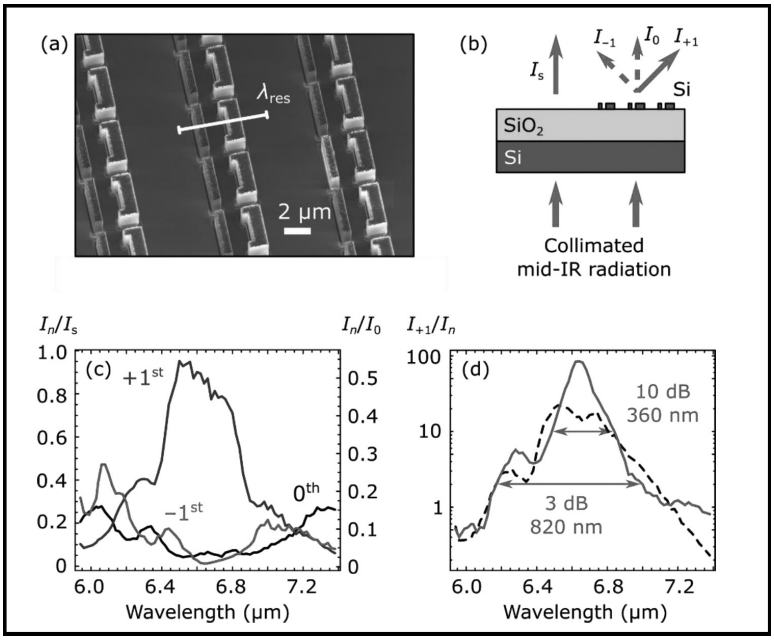

Figure 1: (a) SEM image of the best-performance metagrating. (b) Schematic of the experiment. The three measured diffraction orders in transmission, and the bare substrate transmission, are indicated by arrows. The targeted diffractive order is the $^{+}1^{st}$. (c) Diffraction efficiency of the $^{+}1^{st}$, 0^{th} and $^{-}1^{st}$ transmitted diffraction orders normalized to the bare substrate transmission measured as the function of the wavelength. The axis on the right shows absolute diffraction efficiency as normalized to the incident field intensity. (d) Diffraction contrast spectra I_{+1}/I_0, (dashed line) and I_{+1}/I_{-1} (solid line).

The normalized diffraction efficiency I_{+1}/I_s of the fabricated metagratings, defined as the ratio of the transmission I_{+1} into the targeted diffraction order to the transmission I_s through the bare Si/SiO_2 substrate, was experimentally measured. Such normalization is necessary because of the substantial (43%) amount of light experiencing reflection at the high-contrast flat Si-air and Si-SiO_2 interfaces. This artefact is due to the chosen material platform (SOI), and can be overcome by using, for example, Si-on-sapphire wafers.

A quantum cascade laser (Daylight Solutions MIRcat) was used as a source of highly collimated monochromatic tunable quasi-CW mid-IR radiation, as shown in Figure 1(b). The laser beam was softly focused with a 50-mm-focal-length lens to a 200 μm diameter spot from the back side of the wafer. The intensity of the diffracted light was measured using a pyroelectric array camera (Ophir Spiricon Pyrocam III) by integrating the intensity over the entire array. For each wavelength, the intensities of the $^{+}1^{st}$, $^{-}1^{st}$ and 0^{th} transmitted diffraction orders (I_{+1}, I_{-1}, and I_0) were detected, and the $^{+}1^{st}$ and $^{-}1^{st}$ orders were also detected studied in reflection. The reflected diffraction orders were beyond detection limit. The bare substrate transmission I_s for the efficiency normalization of the diffracted orders was measured by passing the beam through the unstructured part of the wafer, where the device layer is etched away.

The normalized diffraction efficiencies for all transmitted diffraction orders are plotted in Figure 3(c) as a function of the incident wavelength of light. Within our experimental margin of error, the peak grating efficiency at 6.45 μm is of order 95%. Note from Figure 1(c) that the diffraction efficiency into the $^{-}1^{st}$ order is even smaller than into the 0th order. Such an enormous asymmetry between the $^{-}1^{st}$ and $^{+}1^{st}$ orders is due to the bianisotropic nature of the metasurface.

Another important characteristic of the diffraction efficiency is the contrast between the $^{+}1^{st}$ and 0^{th} orders, defined as I_{+1}/I_0, and the $^{+}1^{st}$ and $^{-}1^{st}$ orders, defined as I_{+1}/I_{-1}.

The plots of these quantities shown in Figure 1(d) indicate that the contrasts approach 20 and 80, respectively. Note that the high contrast is achieved for a fairly broad band of mid-IR wavelengths: 260 nm for 10 dB rejection, and 820 nm for the 3 dB rejection of the $^{-}1^{st}$ diffraction order.

References:

[1] Z. Fan, M.R. Shcherbakov, M. Allen, J. Allen, G. Shvets, "Perfect Diffraction with Bianisotropic Metagratings," arXiv:1802.01269 (2018).

Optical Masks for Imaging Exoplanets with Large Ground-Based Telescopes

CNF Project Number: 2499-16

Principal Investigator: Dr. Nemanja Jovanovic

Users: Christopher Alpha, Jeremy Clark, John Treichler, Nemanja Jovanovic, Olivier Guyon, Julien Lozi, Justin Knight

Affiliations: Research Corporation of the University of Hawaii; Subaru Telescope Project; University of Arizona; Cornell NanoScale Facility, Cornell University

Primary Sources of Research Funding: Subaru Telescope Project; Mt. Cuba Foundation

Contact: jovanovic.nem@gmail.com, alpha@cnf.cornell.edu, clark@cnf.cornell.edu, treichler@cnf.cornell.edu, guyon@naoj.org, lozi@naoj.org, jknight@optics.arizona.edu

Primary CNF Tools Used: ASML DUV stepper, Oxford ICE-RIE etcher

Abstract:

A stellar coronagraph is a telescope instrument that enables direct imaging of extra-solar, or exoplanets, from the ground or in space. Some components of the coronagraph system we use require microfabrication techniques to be manufactured. We report on the progress of fabricating optical masks known as complex focal plane masks for stellar coronagraphs, as well as their uses at the Subaru telescope so far.

Summary of Research:

In recent years, astronomers have used telescopes attached with instruments to estimate that approximately 50% of stars have a habitable planet (an Earth-size planet with surface temperature able to sustain liquid water). Current detection limits only allow for the radius, orbit and mass of the planet; identifying if life has developed on the planet requires direct imaging and spectroscopy. This is extremely challenging: the planet can be about a billion times fainter than the star it orbits and is located very close to it on the sky. The key to performing direct imaging and spectroscopy is a telescope instrument called a stellar coronagraph. A stellar coronagraph is designed to access light from the planet for observation by blocking, reducing, or in some way suppressing incoming starlight using a series of carefully designed optical masks.

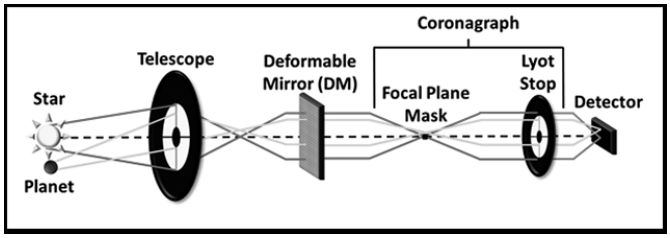

Figure 1. A stellar coronagraph. After entering the telescope, light from the planet passes through the chain of optical masks (focal plane mask, Lyot stop) unchanged, while the starlight is altered in amplitude and phase to allow the collection of planet light from the detector. The deformable mirror can be used to improve the performance of the coronagraph. Image courtesy of Kelsey Miller, University of Arizona.

Each mask is responsible for changing the starlight amplitude and phase to induce deep destructive interference, or cancellation, of the starlight to collect the planet signal possibly buried underneath. A simple coronagraph architecture is shown in Figure 1. It consists of optics after the telescope which focus and collimate the incoming beam at various points; doing so allows for the optical masks to suppress the starlight as discussed.

The stellar coronagraph we developed for the Subaru Coronagraphic Extreme Adaptive Optics (SCExAO) bench at the Subaru Telescope on Mauna Kea, HI, is known as the Phase-Induced Amplitude Apodization Complex-Mask Coronagraph (PIAACMC). It consists of several custom-fabricated optical masks including a "complex" focal plane mask. Figure 2 shows an example of a fabricated complex mask designed to modulate the amplitude and phase of starlight coming to a focus. The fabrication process for this mask used the ASML DUV stepper and an Oxford ICP-RIE etcher.

These masks consist of a tessellated pattern of hexagonal zones which vary in height; the hexagons are responsible for producing the destructive interference of the starlight

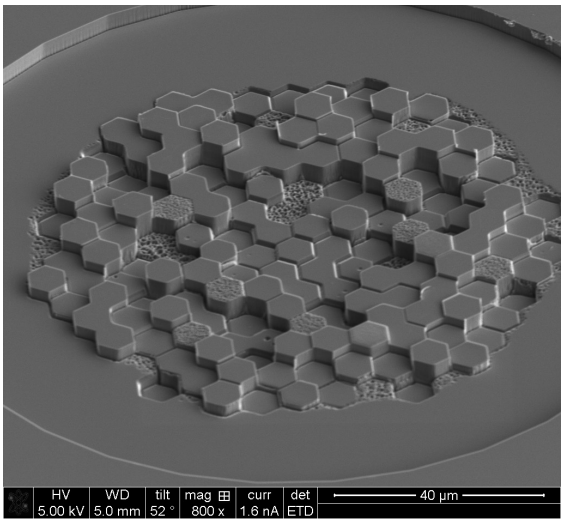

Figure 2: An early iteration of a fabricated complex mask.

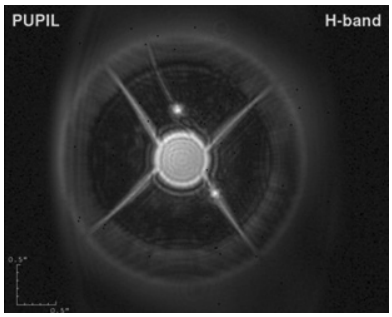

Figure 3: An image of a fabricated complex-mask aligned at SCExAO in the plane before the Lyot stop. Starlight passing through the complex-mask has been changed, but still propagates through to the features of the telescope architecture. This light will be blocked by the Lyot stop, after which the performance of the coronagraph can be measured.

on a detector. This type of focal plane mask must be fabricated using microfabrication techniques as each hexagon is typically on the order of 10 μm wide and a few microns or less deep. Tolerances of these devices are being investigated, but the better they are made to match the original design, the better they can destructively interfere starlight at several wavelengths simultaneously.

The masks from this fabrication effort will be installed and tested at SCExAO soon, but for now only some other masks have been put into the system. Figure 3 demonstrates the intended effect an aligned focal plane mask has in only allowing light to gather in places where it can be blocked by another optical mask. We report on some of these activities in references [1] and [2].

References:

[1] Julien Lozi, et al., "SCExAO: new high-performance coronagraphs ready for science," Proc. SPIE 10706, Advances in Optical and Mechanical Technologies for Telescopes and Instrumentation III, (Publication pending).

[2] Justin M. Knight, John Brewer, Ryan Hamilton, Karen Ward, Tom D. Milster, Olivier Guyon, "Design, fabrication, and testing of stellar coronagraphs for exoplanet imaging," Proc. SPIE 10400, Techniques and Instrumentation for Detection of Exoplanets VIII, 104000N (12 September 2017).

Description of the Exploratory Etching and Electrodeposition Project

CNF Project Number: 2527-17
Principal Investigator: Dr. David Crouse
User: Golsa Mirbagheri

Affiliation: Electrical and Computer Engineering Department, Clarkson University
Primary Source of Research Funding: CFM
Contact: dcrouse@clarkson.edu, mirbagg@clarkson.edu
Primary CNF Tools Used: Oxford 82, Oxford 100, ASML, Gamma, PECVD, Cobra

Abstract:

This project is a continuing project. We will be finishing the fabrication of the hyperbolic metamaterial structure and designing a 2nd generation of the filter that uses more of a photonics crystal resonant material within a Bragg stack. Both the hyperbolic metamaterial structure and the 2nd generation devices have compelling properties. Both show very little dispersion — meaning that their performance is not affected by the angle of incidence to the optical signal.

Project Description:

During the last year, we have further designed the hyperbolic metamaterial device and have performed much more optimization, and have taken into account practical design considerations. We are now fabricating the structure at the Cornell NanoScale Science and Technology Facility (CNF) at Cornell University. We have developed a fabrication plan and are now implementing the plan, with masks designed and fabrication processes in development.

Based on what we have learned, we are now investigating a 2nd generation device that does not use metal wires, but uses resonant cavities in the three middle layers of the Bragg stack. The resulting structure will have far less polarization dependence, will absorb less radiation, will be far easier to fabricate and manufacture, and will have a larger tuning range that allows for it to be used within pixelated wavelength filters for hyperspectral imaging applications.

We have been performing preliminary testing on the resonant cavities and have a preliminary design for operation in the midwavelength infrared range of 3-5 μm. The Bragg stack will use silicon and silicon dioxide, and potentially silicon nitride — all CMOS compatible devices — as well as having all structure features with sizes amenable to optical lithography.

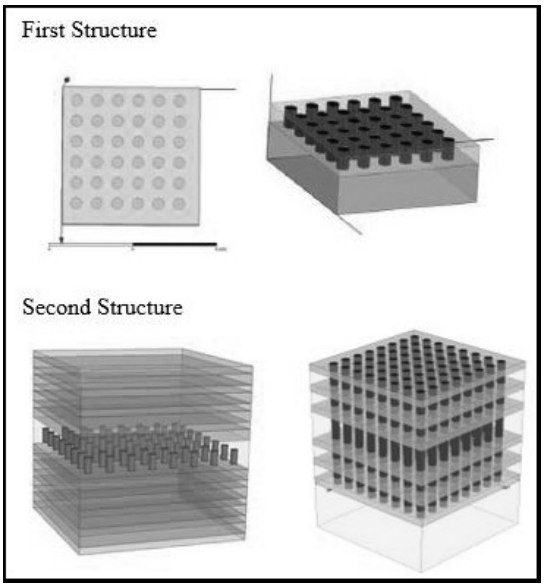

Figure 1: Schematic. Top, First Structure: The 1.5 μm SiO_2 film was deposited, patterned and etched. The holes were 0.5 μm, electroplated with Cu. Bottom, Second Structure: Alternative layers of SiO_2 and Si are deposited, patterned and etched (all through the layers), then holes electroplated with Cu.